



# On axisymmetric/diamond-like mode transitions in axially compressed core–shell cylinders

Fan Xu <sup>a,b,\*</sup>, Michel Potier-Ferry <sup>b</sup>

<sup>a</sup> Institute of Mechanics and Computational Engineering, Department of Aeronautics and Astronautics, Fudan University, 220 Handan Road, Shanghai 200433, PR China

<sup>b</sup> Laboratoire d'Etude des Microstructures et de Mécanique des Matériaux, LEM3, UMR CNRS 7239, Université de Lorraine, Ile du Saulcy, 57045 Metz Cedex 01, France

## ARTICLE INFO

### Article history:

Received 27 November 2015

Received in revised form

7 April 2016

Accepted 18 April 2016

Available online 22 April 2016

### Keywords:

Post-buckling

Bifurcation

Core–shell cylinder

Axisymmetric pattern

Diamond-like pattern

Path-following technique

## ABSTRACT

Recent interests in curvature- and stress-induced pattern formation and pattern selection motivate the present study. Surface morphological wrinkling of a cylindrical shell supported by a soft core subjected to axial compression is investigated based on a nonlinear 3D finite element model. The post-buckling behavior of core–shell cylinders beyond the first bifurcation often leads to complicated responses with surface mode transitions. The proposed finite element framework allows predicting and tracing these bifurcation portraits from a quantitative standpoint. The occurrence and evolution of 3D instability modes including sinusoidally deformed axisymmetric patterns and non-axisymmetric diamond-like modes will be highlighted according to critical dimensionless parameters. Besides, the phase diagram obtained from dimensional analyses and numerical results could be used to guide the design of core–shell cylindrical systems to achieve the desired instability patterns.

© 2016 Elsevier Ltd. All rights reserved.

## 1. Introduction

Morphological wrinkling of a soft material with a stiff thin surface layer has been widely observed in nature such as wrinkles of hornbeam leaf and human skin, and these phenomena have raised considerable research interests during past years (Mahadevan and Rica, 2005; Efimenko et al., 2005). In modern industry, surface wrinkles can be widely applied in many areas ranging from the micro/nano-fabrication of flexible electronic devices with controlled morphological patterns (Bowden et al., 1998; Rogers et al., 2010), the design of coated materials or living tissues (Brau et al., 2011), to the mechanical property measurement of material characteristics (Howarter and Stafford, 2010). Several theoretical, numerical and experimental works have been devoted to stability analyses in order to determine the critical conditions of instability and the corresponding wrinkling patterns (Shield et al., 1994; Steigmann and Ogden, 1997; Cai and Fu, 2000; Chen and Hutchinson, 2004; Huang et al., 2005; Song et al., 2008; Audoly and Boudaoud, 2008). Although linear perturbation analyses can predict the wavelength at the initial stage of instability threshold, determination of the post-bifurcation response and mode transition of surface wrinkles really requires nonlinear buckling analyses. During post-buckling, the wavelength and amplitude of wrinkles will vary with respect to externally applied compressive load. Due to its well-known difficulty, most

\* Corresponding author at: Institute of Mechanics and Computational Engineering, Department of Aeronautics and Astronautics, Fudan University, 220 Handan Road, Shanghai 200433, PR China. Tel.: +86 21 65642737.

E-mail addresses: [fanxu@fudan.edu.cn](mailto:fanxu@fudan.edu.cn) (F. Xu), [michel.potier-ferry@univ-lorraine.fr](mailto:michel.potier-ferry@univ-lorraine.fr) (M. Potier-Ferry).

post-buckling analyses have recourse to computational approaches, especially through using finite element method (Cao and Hutchinson, 2012; Sun et al., 2012; Zang et al., 2012; Xu, 2014; Xu et al., 2014, 2015a, 2015b; Xu and Potier-Ferry, 2016), since only a limited number of exact analytical solutions can be obtained in very simple or simplified cases. In addition, most previous works are concerned with planar film/substrate systems and suggest that wrinkling patterns strongly depend on the applied stresses (Xu et al., 2014, 2015b). However, recent computational and experimental investigations reveal that wrinkling patterns may also vary with the substrate curvature (Yin et al., 2009; Chen and Yin, 2010; Breid and Crosby, 2013; Terwagne et al., 2014) and the wrinkling process under curvature constraints becomes promising techniques for micro/nano-scale surface patterning fabrication (Chan and Crosby, 2006) as well as adaptive aerodynamic drag control (Terwagne et al., 2014). Curvature-induced wrinkling pattern formation and mode selection are only lately being pursued theoretically, numerically and experimentally (Li et al., 2011; Zhao et al., 2014; Stoop et al., 2015; Jia et al., 2015), which demonstrates the important role played by the topological constraints of curved surfaces on instability patterns. For instance, considering a core-shell soft cylinder subjected to axial compression, when the shell is much stiffer than the core, surface wrinkles usually form in both axial and circumferential directions due to topological constraints of curved surfaces, leading to the formation of a non-axisymmetric diamond-like mode (Zhao et al., 2014) instead of sinusoidal wrinkles often observed in planar film/substrate systems under uniaxial compression (Xu et al., 2014, 2015a). This implies that the uniaxial compression can cause two-dimensional instability modes due to the curvature and modulus effects in core-shell cylindrical systems. Nevertheless, the prediction and tracing of the whole pattern evolution on the equilibrium path and the mode transition on curved surfaces in core-shell cylindrical structures represents a challenging numerical issue due to its complicated nonlinear responses and merits much further efforts.

Historically, the nonlinear buckling analysis of thin-walled circular cylindrical shells under various loading conditions has received considerable attentions, the most representative case being the axial compression loading. Cylindrical shells under axial compression are characterized by a high buckling stress ( $\sigma_{cr} = 0.605Eh/R$ ), short wavelength instability patterns ( $\ell \approx \sqrt{Rh}$ ) and a very strong imperfection-sensitivity associated with an extremely unstable post-buckling behavior. The importance of this nonlinear post-bifurcation property has been recognized since 1940s (von Kármán and Tsien, 1941; Koiter, 1945). In the simplest bifurcation analysis, many buckling modes coincide, including axisymmetric and diamond-like shapes. According to Yamaki (1984), localized modes generally first appear in the case of a perfect cylinder, which is due to additional compressive stresses near the boundary. Thus, there are significant differences between flat and curved structures. In the literature, the curvature effect is often accounted through the dimensionless Batdorf parameter  $Z = L^2(1 - \nu^2)/(Rh)$  (Yamaki, 1984; Bushnell, 1985; Abdelmoula et al., 1992; Abdelmoula and Leger, 2008). However, when a cylindrical shell is filled with a soft core, i.e. a core-shell soft cylinder, the short wavelength bifurcation modes can be persistently observed experimentally and numerically in both buckling and post-buckling range (Zhao et al., 2014), and the unstable post-bifurcation behavior can be altered by the presence of a core. In this paper, the dimensionless parameters characterizing a core-shell cylindrical system will be highlighted. There exist numerous references on the buckling of circular cylindrical shells, which is rather difficult to quote comprehensively. Here we only refer to a few textbooks (Yamaki, 1984; Bushnell, 1985; Julien, 1991; Teng and Rotter, 2006; Koiter, 2009), review papers (Hutchinson and Koiter, 1970; Arbocz, 1987; Teng, 1996) and a website named "Shell Buckling" (Bushnell and Bushnell, 2015). In addition, there also exist a few contributions on the buckling analyses of a cylindrical shell filled with a soft core, either studying the stabilizing effects of soft cores on the buckling strength of shells (Yao, 1962; Myint-U, 1969) or focusing on axisymmetric instability modes (Karam and Gibson, 1995; Ye et al., 2011; Wu et al., 2012).

This study aims at exploring the occurrence and post-buckling evolution of 3D wrinkling patterns in core-shell soft cylindrical structures subjected to axial compression, through applying advanced numerical methods from a quantitative standpoint. A theoretical analysis based on the nonlinear Donnell–Mushtari–Vlassov (DMV) shell equations is first carried out to qualitatively determine the critical dimensionless parameters that influence the instability patterns. Spatial pattern formation is then quantitatively investigated based on a nonlinear 3D finite element model associating geometrically nonlinear shell formulations for the surface layer and linear elastic solids for the core. The model incorporates Asymptotic Numerical Method (ANM) (Damil and Potier-Ferry, 1990; Cochelin et al., 1994, 2007; Cochelin, 1994) as a robust path-following technique to predict a sequence of secondary bifurcations on their post-buckling evolution path as the load is increased. In this paper, we consider geometrically perfect core-shell cylinders without any imperfection. The numerical path-following method is employed to trace the whole post-buckling evolution in bifurcation diagrams and to describe the phase diagrams (axisymmetric/diamond-like modes) according to those critical dimensionless parameters.

This paper explores the occurrence and post-buckling evolution of 3D instability modes including axisymmetric and non-axisymmetric diamond shaped patterns in greater depth. The paper is organized as follows. In Section 2, a theoretical analysis based on the DMV shell equations is performed to find the critical parameter that determines the axisymmetric/diamond-like instability patterns. In Section 3, a nonlinear finite element model is developed for core-shell cylindrical systems. Then in Section 4, the resulting nonlinear problem is reformulated by the ANM algorithm as a path-following continuation technique. Results and discussions are provided in Section 5, including the onset and evolution of the sinusoidally deformed axisymmetric pattern and the non-axisymmetric diamond-like one. Concluding remarks are given in Section 6.

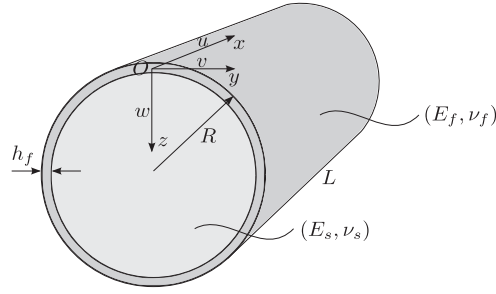


Fig. 1. Geometry of core-shell cylindrical structure.

## 2. Theoretical analysis

The core-shell cylindrical systems will be qualitatively discussed to highlight the main features of the non-linear behavior of this structure subjected to axial compression. The analyses are conducted within the framework of Donnell–Mushtari–Vlassov (DMV) shell equations that appear to be the simplest model for cylindrical thin-walled structures (Yamaki, 1984). It is known that this model offers good results in the cases of short-wavelength instability, which generally occurs under axial compression situation. For other loads like external pressure, the DMV shell model may be inaccurate, but it can provide consistent orders of magnitude for the critical stress and wavelength, which is sufficient for the analyses in this section. Nevertheless, nonlinear calculations in the following computational sections will be carried out based on a nonlinear shell model that is valid for large rotations and large displacements to describe any buckling mode.

### 2.1. Core-shell modeling within the DMV framework

We consider an elastic cylindrical shell supported by a soft core, which can buckle under axial compression. Upon wrinkling, the shell elastically buckles to relax the compressive stress and the core concurrently deforms to maintain perfect bonding at the interface. The core-shell cylindrical system is considered to be three-dimensional and the geometry is as shown in Fig. 1. In this study, we consider the case where the thickness of the shell is much smaller than the radius of the cylinder. In this theoretical part, let  $x$  and  $y$  be axial and circumferential coordinates, while  $z$  represents the radial direction coordinate. The thickness of the shell, the radius and the length of the system are denoted by  $h_f$ ,  $R$  and  $L$ , respectively. Young's modulus and Poisson's ratio of the shell are respectively denoted by  $E_s$  and  $\nu_s$ , while  $E_f$  and  $\nu_f$  are the corresponding material properties for the core. The same frame will be adapted to the components of the displacements  $u$ ,  $v$ ,  $w$ , the resultant membrane stress  $\mathbf{N}$ , the bending moment  $\mathbf{M}$ , the membrane strain  $\gamma$  and the curvature tensor  $\mathbf{K}$ . Within the DMV framework (Yamaki, 1984), the shell strains are approximated as

$$\begin{cases} \gamma_x = \frac{\partial u}{\partial x} + \frac{1}{2} \left( \frac{\partial w}{\partial x} \right)^2, & \gamma_y = \frac{\partial v}{\partial y} + \frac{1}{2} \left( \frac{\partial w}{\partial y} \right)^2 - \frac{w}{R}, & \gamma_{xy} = \frac{\partial u}{\partial y} + \frac{\partial v}{\partial x} + \frac{\partial w}{\partial x} \frac{\partial w}{\partial y}, \\ k_x = -\frac{\partial^2 w}{\partial x^2}, & k_y = -\frac{\partial^2 w}{\partial y^2}, & k_{xy} = -2 \frac{\partial^2 w}{\partial x \partial y}. \end{cases} \quad (1)$$

As compared with the Föppl–von Kármán nonlinear plate model, only the strain  $\gamma_y$  has been changed to account for the circumferential stretching due to the deflection  $w$  and this new term plays a key role in shell buckling. The elastic energy of the shell can be written in a classical form

$$\Pi_f = \Pi_{ben} + \Pi_{mem} = \frac{1}{2} \iint_{\Omega_f} (D^f \mathbf{K} \cdot \mathbf{K} + J^f \gamma \cdot \gamma) dx dy, \quad (2)$$

where  $D = E_f h_f^3 / [12(1 - \nu_f^2)]$  and  $J = E_f h_f / (1 - \nu_f^2)$  stand for the flexural and extensional rigidities of the shell, respectively. The dimensionless elastic matrix  $\mathbf{L}_f$  is defined as

$$\mathbf{L}_f = \begin{bmatrix} 1 & \nu_f & 0 \\ \nu_f & 1 & 0 \\ 0 & 0 & \frac{1 - \nu_f}{2} \end{bmatrix}. \quad (3)$$

As often considered in film/substrate systems (Chen and Hutchinson, 2004; Audoly and Boudaoud, 2008; Xu et al., 2014, 2015b), we assume that the core can be governed by small strain elasticity so that the potential energy is given by

$$\Pi_s = \frac{1}{2} \iiint_{\Omega_s} {}^t\mathbf{e} \cdot \mathbf{L}_s \cdot \mathbf{e} \, dx \, dy \, dz. \quad (4)$$

This elastic behavior of the core can also be represented by a Winkler-type foundation:

$$\Pi_s = \frac{1}{2} \iint_{\Omega_s} K_s w^2 \, dx \, dy. \quad (5)$$

It has been established (Biot, 1937; Allen, 1969) that the core stiffness  $K_s$  depends on the half buckled wavelength  $\ell_x$ :

$$K_s = \frac{2E_s \pi}{(3 - \nu_s)(1 + \nu_s)} \frac{1}{\ell_x}. \quad (6)$$

The important point in the dimensional analysis below is the order of magnitude  $K_s \sim E_s/\ell_x$ .

## 2.2. Axisymmetric buckling

According to Zhao et al. (2014), the instability pattern of core-shell cylindrical systems can be axisymmetric or diamond shaped. We begin with axisymmetric modes under axial compression:  $\nu=0$ ,  $u$  and  $w$  are only functions of  $x$ ,  $N_x = -\sigma h$ , where the axial compressive stress  $\sigma$  is prescribed. This classical analysis is revisited here to highlight the dimensionless parameters influencing the behavior of axially compressed core-shell cylinders. As compared to planar structures, the main difference lies in the azimuthal stress  $\gamma_y = -w/R$  that induces a large transversal stiffness. The total elastic energy of the core-shell cylinder is then simplified as

$$\Pi = \frac{1}{2} \int_{\Omega} \left( D \left( \frac{d^2 w}{dx^2} \right)^2 + J \frac{w^2}{R^2} + K_s w^2 + J \gamma_x^2 - 2J \nu_f \gamma_x \frac{w}{R} \right) dx. \quad (7)$$

For a shell without a core, i.e.  $K_s=0$ , the buckling wavelength is such that the two first terms of this energy are of the same order (bending energy vs. transversal membrane energy), which leads to

$$\frac{1}{\ell_x^4} \sim \frac{J}{DR^2} \sim \frac{1}{R^2 h_f^2} \Rightarrow \ell_x \sim \sqrt{Rh_f}. \quad (8)$$

The influence of the core can be represented by the ratio between the second and the third terms in Eq. (7), which results in the definition of a dimensionless parameter  $K_s R^2/J \sim (E_s/E_f)[R^2/(\ell_x h_f)]$ . If the instability wavelength remains of the same order of magnitude as for the pure shell, it naturally leads to a new dimensionless parameter that is a measure of the core stiffness compared with the shell membrane stiffness:

$$C_s = \frac{E_s}{E_f} \left( \frac{R}{h_f} \right)^{3/2}. \quad (9)$$

A differential equation can be associated with the functional (7) (see Yamaki, 1984):

$$D \frac{d^4 w}{dx^4} + \sigma h_f \frac{d^2 w}{dx^2} + \left( \frac{E_f h_f}{R^2} + K_s \right) w + \frac{\nu_f \sigma h_f}{R} = 0, \quad (10)$$

$$N_x = -\sigma h_f, \quad N_y = -\nu_f \sigma h_f - \frac{E_f h_f}{R} w, \quad N_{xy} = 0. \quad (11)$$

First, let us remark that the same dimensionless coefficient  $K_s R^2/(E_f h_f)$  appears in the third term of (10). Second, Eq. (10) becomes linear, which means that the bifurcated branch is neither supercritical nor subcritical. In the absence of the core, i.e.  $K_s=0$ , harmonic solutions of the homogeneous axisymmetric problem (1) lead to the classical buckling stress of an axially compressed circular cylindrical shell and its corresponding wavelength:

$$\begin{cases} \sigma_{cr} = \frac{1}{\sqrt{3(1-\nu_f^2)}} \frac{E_f h_f}{R} \sim 0.605 \frac{E_f h_f}{R} & \text{when } \nu_f = 0.3, \\ \frac{\ell_x}{\pi} = \frac{\sqrt{Rh_f}}{[12(1-\nu_f^2)]^{1/4}}. \end{cases} \quad (12)$$

This well-known result assumes a uniaxial pre-buckling stress and neglects boundary effects. If one considers the boundary condition  $w=0$ , the exact solution of (10) includes a boundary layer with the length  $\sqrt{Rh_f}$  where the azimuthal stress is compressive, which causes non-axisymmetric buckling modes localized in the boundary layer (Yamaki, 1984). Such localized wavy patterns will be recovered in some cases with a soft core. Third, the axisymmetric buckling analysis is slightly more intricate in the presence of a soft core since the core stiffness  $K_s$  depends on the wavelength (Biot, 1937; Karam and Gibson, 1995), but clearly the core stiffness increases the buckling stress and decreases the wavelength. Last, it is well known that

axially compressed cylindrical shells are extremely imperfection-sensitive (Koiter, 1945; Hutchinson and Koiter, 1970; Koiter, 2009) due to the existence of unstable solution branches much earlier than the analytical buckling load  $\sigma_{cr}$ . We can wonder if this very unstable behavior remains in the presence of a core.

In analyses of a cylindrical shell without a core, the famous Batdorf parameter  $Z = L^2(1 - \nu_f^2)/(Rh_f)$  is often taken into account. It is quite simple to use the ratio  $L/\ell_x \approx L/\sqrt{Rh_f} \approx \sqrt{Z}$  to measure the wave number. In practice this number is often large ( $Z \sim 500$ ). When it becomes quite small ( $Z$  is in the range  $20 \sim 50$ ), the influence of the boundary conditions extends to the whole structure, while this effect is constrained to the boundary layers for large values of the Batdorf parameter. For a thorough analysis of these boundary layers in the case of an external pressure loading, see Abdelmoula and Leger (2008). Hence, we have two main dimensionless parameters,  $C_s$  and  $Z$ , to characterize the axisymmetric response of compressed core-shell cylinders. The question remained now tends to find out the number of characteristic parameters for a general response that can be axisymmetric or not.

### 2.3. Dimensional analysis

To find the dimensionless parameters characterizing core-shell cylindrical systems, we start from the elastic energies,  $\Pi_f$  and  $\Pi_s$ , respectively defined in (2) and (4), associating the DMV shell equations for the surface layer and a 3D small strain model for the core. We can introduce some dimensionless coordinates and non-dimensional kinematic variables as follows:

$$\begin{cases} (x, y, z) = \ell_x(\bar{x}, \bar{y}, \bar{z}), & \ell_x = \sqrt{Rh_f}, \\ (u, v) = \frac{h_f^2}{R}(\bar{u}, \bar{v}), & w = h_f\bar{w}. \end{cases} \quad (13)$$

This implies that the deflection  $w$  is of the order of the thickness  $h_f$ , while the other components of the displacements are much smaller, in the order of  $h_f^2/R$ . This scaling is quite classical within the plate and shell theory (Yamaki, 1984). The hypothesis of a single length scale in the physical space deserves a serious discussion. For instance, in the case of buckling under external pressure, the length scales are not always the same in the  $x$  and  $y$  directions (Abdelmoula et al., 1992; Abdelmoula and Leger, 2008). However, in the case of an axial compression loading, the possible wave numbers are located on the famous Koiter circle (Koiter, 1945), which suggests that the two wave numbers can be of the same order of magnitude. This has been confirmed by a number of experiments and numerical calculations that generally mention diamond shaped patterns. In the case of planar film/substrate systems, there exist exact solutions proving that the transverse characteristic length is also of the same order (Biot, 1937; Xu et al., 2015b). From Eq. (13), one can obtain all the components of the mean strain and the curvature being of the same order:

$$\begin{cases} (\gamma_x, \gamma_y, \gamma_{xy}) = \frac{h_f}{R}(\bar{\gamma}_x, \bar{\gamma}_y, \bar{\gamma}_{xy}), \\ (k_x, k_y, k_{xy}) = \frac{1}{R}(\bar{k}_x, \bar{k}_y, \bar{k}_{xy}), \end{cases} \quad (14)$$

where the dimensionless strain and curvature tensors are expressed in terms of the dimensionless coordinates and displacement components in the shell exactly described by the same formulae as in (1). As for the strain in the core, it involves two orders of magnitude since the transversal displacement is assumed to be larger than the two other components, which leads to

$$(\varepsilon_x, \varepsilon_y, \varepsilon_z, 2\varepsilon_{yz}, 2\varepsilon_{xz}, 2\varepsilon_{xy}) = \left(\frac{h_f}{R}\right)^{1/2} \left(0, 0, \frac{\partial \bar{w}}{\partial \bar{z}}, \frac{\partial \bar{w}}{\partial \bar{y}}, \frac{\partial \bar{w}}{\partial \bar{x}}, 0\right) + \left(\frac{h_f}{R}\right)^{3/2} \left(\frac{\partial \bar{u}}{\partial \bar{x}}, \frac{\partial \bar{v}}{\partial \bar{x}}, 0, \frac{\partial \bar{v}}{\partial \bar{z}}, \frac{\partial \bar{u}}{\partial \bar{z}}, \frac{\partial \bar{u}}{\partial \bar{y}} + \frac{\partial \bar{v}}{\partial \bar{x}}\right). \quad (15)$$

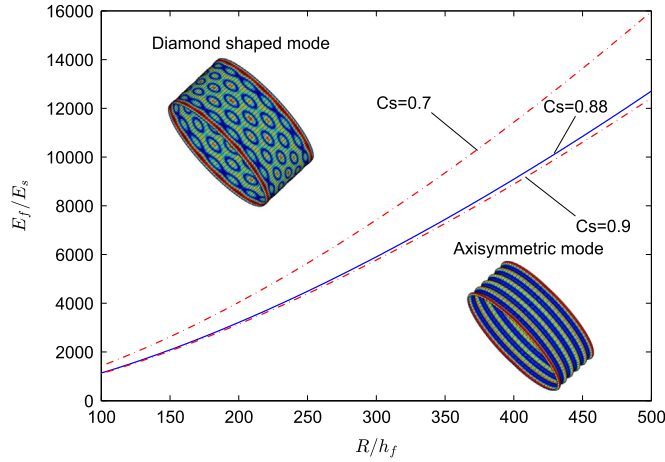
From Eqs. (14) and (15) as well as the assumption of the wavelength  $\ell_x = \sqrt{Rh_f}$ , it appears that the membrane and bending energies are of the same order. The order for the shell energy and the corresponding one for the core respectively read

$$\begin{cases} \frac{\Pi_f}{\ell_x^2} \sim \frac{E_f h_f^3}{R^2}, \\ \frac{\Pi_s}{\ell_x^2} \sim \frac{E_s h_f \ell_x}{R} = \frac{E_s h_f^{3/2}}{R^{1/2}}. \end{cases} \quad (16)$$

Thus, the energy ratio  $\Pi_s/\Pi_f$  results in the same parameter as for the axisymmetric buckling analysis above:

$$C_s = \frac{E_s h_f^{3/2}/R^{1/2}}{E_f h_f^3/R^2} = \frac{E_s}{E_f} \left(\frac{R}{h_f}\right)^{3/2}. \quad (17)$$

There exist two other dimensionless parameters from the domain occupied by the dimensionless variables:



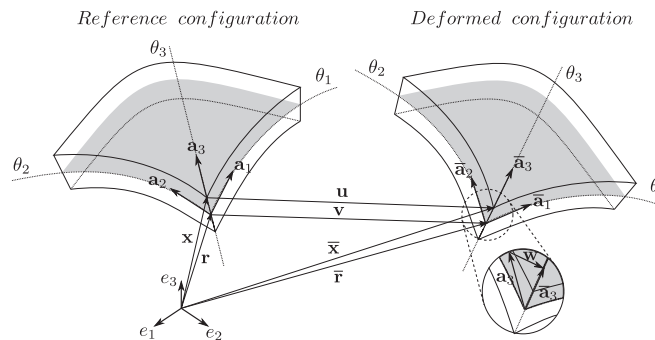
**Fig. 2.** A phase diagram on pattern selection defined by Eq. (17). The blue solid curve is determined by the critical parameter  $C_s = 0.88$ , which corresponds to the two critical ratios,  $R/h_f$  and  $E_f/E_s$ , respectively chosen as (125, 1600) and (200, 3200) in Zhao et al. (2014). The two red dash-dot curves give the upper and lower bounds obtained through the numerical results in Section 5, as supported by Supplementary information. When the critical parameter  $C_s \geq 0.9$ , the instability mode is axisymmetric; whereas at a smaller value  $C_s \leq 0.7$ , the system may branch into the diamond shaped mode. The pattern selection in the narrow region  $0.7 < C_s < 0.9$  appears to be quite sensitive in the numerical results. (For interpretation of the references to color in this figure caption, the reader is referred to the web version of this paper.)

$$\begin{cases} 0 \leq \bar{x} \leq L/\ell_x, \\ 0 \leq \bar{y} \leq \frac{2\pi R}{\ell_x} = 2\pi \left( \frac{R}{h_f} \right)^{1/2}. \end{cases} \quad (18)$$

These two parameters correspond to the wave numbers in the axial and circumferential directions, the first one being related to the Batdorf parameter. Nevertheless, in axially compressed cases, these parameters are generally large and their influence is constrained to the boundary layers so that the main parameter turns out to be  $C_s$ . This suggests the two systems sharing a common  $C_s$  should have the same buckling and post-buckling behavior, the only difference being due to boundary effects and wave numbers in both directions. Most importantly, this critical parameter  $C_s$  can determine a phase diagram (see Fig. 2) on pattern selection, i.e. axisymmetric or diamond-like mode, which well agrees with the analytical solution in Zhao et al. (2014) and our numerical results in Section 5.

### 3. 3D finite element model

The 3D core-shell cylindrical system will be modeled in a rather classical way, the surface layer being represented by a thin shell model to allow large rotations while the core being modeled by small strain elasticity. Indeed, the considered instabilities are governed by nonlinear geometric effects in the stiff material, while these effects are much smaller in the soft material. For planar film/substrate systems, a thorough investigation on comparison between finite strain hyperelastic model and small strain linear elastic model with respect to different stiffness range of Young's modulus was carried out in Xu et al. (2015a). It demonstrates that unless the stiffness ratio is rather small, e.g.  $E_f/E_s \approx O(10)$ , the deformation of the system can be large and so that finite strain models have to be taken into account. In most cases of film/substrate systems,



**Fig. 3.** Geometry and kinematics of shell.



i.e.  $E_f/E_s \gg O(10)$ , small strain elastic models appear to be sufficient and are qualitatively or even quantitatively equivalent to finite strain hyperelastic models. This remains valid for core-shell soft cylindrical structures as well, see Zhao et al. (2014). Therefore, in the following, the elastic potential energy of the system, is considered within the framework of Hookean elasticity for simplicity.

Challenges in the numerical modeling of such core-shell cylindrical systems come from the large aspect ratio ( $2\pi R/h_f \geq O(10^2)$ ,  $L/h_f \geq O(10^2)$ ) and radius/thickness ratio ( $R/h_f \geq O(10^2)$ ), which requires very fine meshes if employing 3D brick elements both for the surface and for the core. Since finite rotations of middle surface and small strains are considered in the surface layer, nonlinear shell formulations are quite suitable and efficient for modeling. In this paper, a 3D shell formulation proposed by Büchter et al. (1994) is applied. It is based on a 7-parameter theory including a linear varying thickness stretch as extra variable, which allows applying a complete 3D constitutive law without condensation. It is distinguished from classical shell models that are usually based on degenerated constitutive relations (e.g. Kirchhoff–Love, Reissner–Mindlin theories). It is also incorporated via the Enhanced Assumed Strain (EAS) concept proposed by Simo and Rifai (1990) to improve the element performance and to avoid locking phenomena such as Poisson thickness locking, shear locking or volume locking. This hybrid shell formulation can describe large rotations and large displacements, and has been successively applied to nonlinear elastic thin-walled structures such as cantilever beam, square plate, cylindrical roof and circular deep arch (Zahrouni et al., 1999; Boutyour et al., 2004).

Geometry and kinematics of the shell element are illustrated in Fig. 3, where the position vectors are functions of curvilinear coordinates ( $\theta^1, \theta^2, \theta^3$ ). The geometry description relies on the middle surface coordinates  $\theta^1$  and  $\theta^2$  of the shell, while  $\theta^3$  represents the coordinate in the thickness direction. The current configuration is defined by the middle surface displacement and the relative displacement between the middle and the upper surfaces. The large rotations are taken into account without any rotation matrix since the current direction vector is obtained by adding a vector to one of the initial configurations.

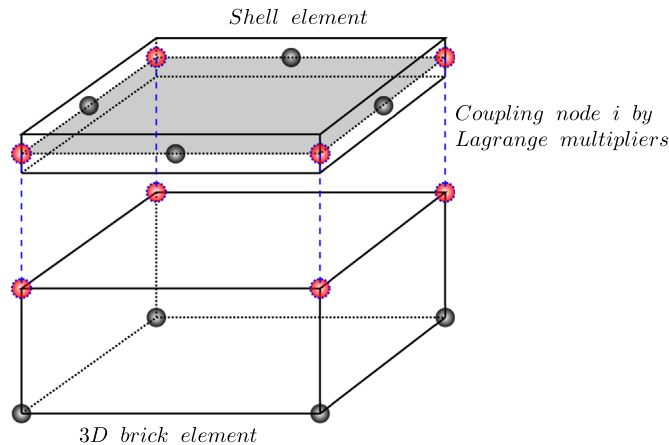
Detailed formulations of geometry and kinematics of the shell element are presented in Appendix A. Finally, the hybrid shell formulation is derived from a three-field variational principle based on the Hu–Washizu functional (Büchter et al., 1994; Zahrouni et al., 1999). The stationary condition can be written as

$$\Pi_f(\mathbf{u}_f, \tilde{\gamma}, \mathbf{S}) = \int_{\Omega_f} \left\{ {}^t\mathbf{S} : (\gamma_u + \tilde{\gamma}) - \frac{1}{2} {}^t\mathbf{S} : \mathbf{D}^{-1} : \mathbf{S} \right\} d\Omega - \lambda \mathbf{P}_{\text{ext}}(\mathbf{u}_f), \quad (19)$$

where  $\mathbf{D}$  is the elastic stiffness tensor. The unknowns are, respectively, the displacement field  $\mathbf{u}_f$ , the second Piola–Kirchhoff stress tensor  $\mathbf{S}$  and the compatible Green–Lagrange strain  $\gamma_u$ . The enhanced assumed strain  $\tilde{\gamma}$ , satisfies the condition of orthogonality with respect to the stress field. The work of external load is denoted by  $\mathbf{P}_{\text{ext}}(\mathbf{u})$ , while  $\lambda$  is a scalar load parameter.

A 8-node quadrilateral element with reduced integration is used for the 7-parameter shell formulation. The enhanced assumed strain  $\tilde{\gamma}$  does not require inter element continuity, neither contribute to the total number of nodal degrees of freedom. Therefore, it can be eliminated by condensation at the element level, which preserves the formal structure of a 6-parameter shell theory with totally 48 degrees of freedom per element.

Since the displacement, rotation and strain remain relatively small in the core, the linear isotropic elasticity theory can accurately describe the core. As mentioned before, the nonlinear strain–displacement behavior has essentially no influence on the results of interest. Hence, the potential energy of the core can be expressed as



**Fig. 4.** Sketch of coupling at the interface. The coupling nodes are marked by red color. (For interpretation of the references to color in this figure caption, the reader is referred to the web version of this paper.)

$$\Pi_s(\mathbf{u}_s) = \frac{1}{2} \int_{\Omega_s} \boldsymbol{\epsilon} : \mathbf{L}_s : \boldsymbol{\epsilon} d\Omega - \lambda \mathbf{P}_{\text{ext}}(\mathbf{u}_s), \quad (20)$$

where  $\mathbf{L}_s$  is the elastic matrix of the core and the strain is denoted as  $\boldsymbol{\epsilon}$ . In this paper, 8-node linear brick elements with reduced integration are applied to discretize the core, with totally 24 degrees of freedom on each brick element.

As the surface shell is bonded to the core, the displacement should be continuous at the interface. However, the shell elements and 3D brick elements cannot be simply joined directly since they belong to dissimilar elements. Therefore, additional incorporating constraint equations have to be employed. Here, Lagrange multipliers are applied to couple the corresponding nodal displacements in compatible meshes between the shell and the core (see Fig. 4). Note that using 8-node linear brick element here is only for coupling convenience, 20-node quadratic brick element would be another good candidate, while both of them follow the same coupling strategy. Consequently, the stationary function of the core–shell system is given in a Lagrangian form:

$$\mathcal{L}(\mathbf{u}_f, \mathbf{u}_s, \ell) = \Pi_f + \Pi_s + \sum_{\text{node } i} \ell_i [\mathbf{u}_{\bar{f}}(i) - \mathbf{u}_s(i)], \quad (21)$$

in which

$$\mathbf{u}_{\bar{f}}(i) = \mathbf{v}(i) - \frac{h_f}{2} \mathbf{w}(i). \quad (22)$$

where the displacements of the shell and the core are respectively denoted as  $\mathbf{u}_f$  and  $\mathbf{u}_s$ , while the Lagrange multipliers are represented by  $\ell$ . At the interface, the displacement continuity is satisfied at the same nodes and connects the inner surface of the shell ( $\mathbf{u}_{\bar{f}}$ ) and the outer surface of the core. From Eq. (21), three equations are obtained according to  $\delta \mathbf{u}_f$ ,  $\delta \mathbf{u}_s$  and  $\delta \ell$ :

$$\begin{cases} \delta \Pi_f + \sum_{\text{node } i} \ell_i \delta \mathbf{u}_{\bar{f}}(i) = 0, \\ \delta \Pi_s - \sum_{\text{node } i} \ell_i \delta \mathbf{u}_s(i) = 0, \\ \sum_{\text{node } i} \delta \ell_i \mathbf{u}_{\bar{f}}(i) - \sum_{\text{node } i} \delta \ell_i \mathbf{u}_s(i) = 0. \end{cases} \quad (23)$$

#### 4. Path-following technique

Asymptotic Numerical Method (ANM) (Damil and Potier-Ferry, 1990; Cochelin et al., 1994, 2007; Cochelin, 1994) is applied to solve the resulting nonlinear equations. The ANM is a path-following technique that is based on a succession of high order power series expansions (perturbation technique) with respect to a well chosen path parameter, which appears as an efficient continuation predictor without any corrector iteration. Besides, one can get approximations of the solution path that are very accurate inside the radius of convergence. In this paper, the main interest of the ANM is its ability to trace the post-buckling evolution on the equilibrium path and to predict secondary bifurcations without any special tool. Precisely, accumulation of small steps in the ANM is often associated with the occurrence of a bifurcation (Xu, 2014; Xu et al., 2014, 2015a, 2015b).

The resulting nonlinear problem (23) can be rewritten as

$$\delta \mathcal{L}(\mathbf{u}_f, \mathbf{u}_s, \ell) = \langle \mathbf{R}(\mathbf{U}, \lambda), \delta \mathbf{U} \rangle = 0, \quad (24)$$

where  $\mathbf{U} = (\mathbf{u}_f, \mathbf{u}_s, \ell)$  is a mixed vector of unknowns and  $\mathbf{R}$  is the residual vector. The external load parameter is denoted as a scalar  $\lambda$ . The principle of the ANM continuation consists in describing the solution path by computing a succession of truncated power series expansions. From a known solution point  $(\mathbf{U}_0, \lambda_0)$ , the solution  $(\mathbf{U}, \lambda)$  is expanded into truncated power series of a perturbation parameter  $a$ :

$$\begin{cases} \mathbf{U}(a) = \mathbf{U}_0 + \sum_{p=1}^n a^p \mathbf{U}_p, \\ \lambda(a) = \lambda_0 + \sum_{p=1}^n a^p \lambda_p, \end{cases} \quad (25)$$

$$a = \langle \mathbf{u} - \mathbf{u}_0, \mathbf{u}_1 \rangle + (\lambda - \lambda_0) \lambda_1, \quad (26)$$

where  $n$  is the truncation order of the series. Eq. (26) defines the path parameter  $a$  that can be identified to an arc-length parameter. By introducing Eq. (25) into Eqs. (24) and (26), then equating the terms at the same power of  $a$ , one can obtain a set of linear problems. More details of these procedures can be found in Cochelin et al. (1994, 2007), Xu et al. (2014, 2015b).



**Table 1**

Material and geometric properties of different core-shell cylindrical structures.

Case	$E_f$ (MPa)	$E_s$ (MPa)	$\nu_f$	$\nu_s$	$h_f$ (mm)	$R$ (mm)	$L$ (mm)	$C_s$
Core-shell I	$1.3 \times 10^3$	1.8	0.4	0.48	$10^{-3}$	0.2	0.2	3.92
Core-shell II	$2.16 \times 10^4$	1.8	0.4	0.48	$10^{-3}$	0.3	0.3	0.43
Core-shell III	$2.16 \times 10^4$	1.8	0.4	0.48	$10^{-3}$	0.113	0.15	0.1
Core-shell IV	$2.16 \times 10^5$	1.8	0.3	0.48	$10^{-3}$	0.113	0.3	0.01

The maximum value of the path parameter  $a$  should be automatically defined by analyzing the convergence of the power series at each step. This  $a_{max}$  can be based on the difference of displacements at two successive orders that must be smaller than a given precision parameter  $\delta$ :

$$\text{Validity range: } a_{max} = \left( \delta \frac{\|\mathbf{u}_1\|}{\|\mathbf{u}_n\|} \right)^{1/(n-1)}, \quad (27)$$

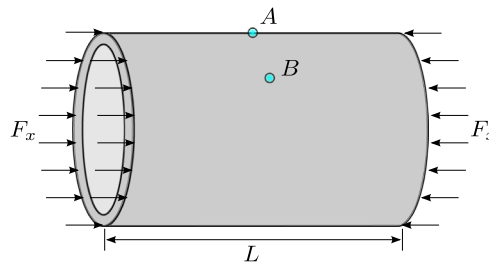
where the notation  $\|\cdot\|$  stands for the Euclidean norm. Unlike incremental-iterative methods, the arc-length step size  $a_{max}$  is adaptive since it is determined *a posteriori* by the algorithm. When there is a bifurcation point on the solution path, the radius of convergence is defined by the distance to the bifurcation. Thus, the step length defined in Eq. (27) becomes smaller and smaller, which looks as if the continuation process "knocks" against the bifurcation (Baguet and Cochelin, 2003). This accumulation of small steps is a very good indicator of the presence of a singularity on the path. All the bifurcations can be easily identified in this way by the user without any special tool.

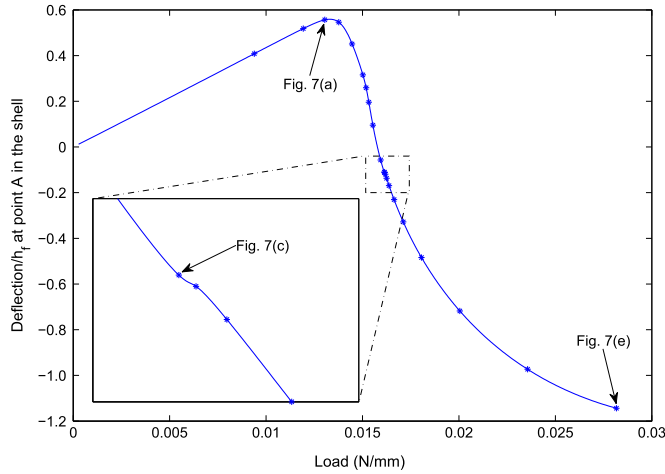
It is worth mentioning that there are only two parameters controlling the algorithm. The first one is the truncation order  $n$  of the series. It was previously discussed that the optimal truncation order should be large enough between 10 and 20, but bigger values (e.g.  $n=50$ ) lead to good results for large-scale problems as well (Medale and Cochelin, 2009). Another important parameter is the chosen tolerance  $\delta$  that affects the residual. For instance, very small values of tolerance (e.g.  $\delta = 10^{-6}$ ) ensure quite a high accuracy and a pretty robust path-following process.

## 5. Results and discussions

Spatial wrinkling pattern formation and evolution of core-shell cylindrical structures subjected to axial compression will be investigated numerically. The computational technique has been chosen to avoid most of the restrictive assumptions on initial geometric imperfections that are generally performed in the literature (Zhao et al., 2014; Jia et al., 2015): here the considered domain is three-dimensional without any geometric imperfection and the path-following technique provides the post-buckling response of the system beyond the primary bifurcation.

The material and geometric properties of the core-shell composite system are chosen according to the phase diagram of Fig. 2, which are similar to those in Zhao et al. (2014) and shown in Table 1. According to the core stiffness parameter  $C_s$  defined in Section 2, pattern selection mainly depends on the geometric and physical parameters: radius/thickness ratio  $R/h_f$  and modulus ratio  $E_f/E_s$ . Hence, various cases with representative geometric and physical properties are considered for the calculations: some of them have a relatively big  $C_s$  while the others may hold a small value (see Table 1 and Supplementary material). Poisson's ratio is a dimensionless measure of the degree of compressibility. Compliant materials in the core, such as elastomers, are nearly incompressible with  $\nu_s = 0.48$ . In this paper, the force loading is applied to the shell and the core is loading free (see Fig. 5). In order to trigger a transition from the fundamental branch to the bifurcated one, a small perturbation force,  $f_z = 10^{-6}$ , is imposed in the shell. The introduction of such small perturbation forces is quite a common technique in the solution of bifurcation problems by continuation techniques (Doedel, 1981; Allgower and Georg, 1990), even when using commercial finite element codes. This artifice could be avoided by applying a specific procedure to compute the bifurcation branch as in Boutyou et al. (2004) and Vannucci et al. (1998). In this paper, the perturbation force  $f_z$  allows the whole bifurcated branch with a single continuation algorithm to be computed. The number of elements required

**Fig. 5.** Core-shell cylinder subjected to axial compression.



**Fig. 6.** Bifurcation curve of Core-shell I with  $C_s = 3.92$  under axial compression. Representative wrinkling shapes in Fig. 7 on the post-buckling evolution path are marked. ANM parameters:  $n = 15$ ,  $\delta = 10^{-4}$ , 21 steps. Each point corresponds to one ANM step.

for a convergent solution was carefully examined. Bifurcation points are detected by the criterion of small step accumulation. Indeed, when the starting point of the step is close to the bifurcation, the radius of convergence of Taylor series coincides with the distance to the singular point, which explains that the continuation process “knocks” against the bifurcation (Baguet and Cochelin, 2003). More advanced techniques are available for bifurcation detection such as bifurcation indicator (Xu et al., 2014, 2015b) and power series analysis (Cochelin and Medale, 2013), but the simple detection by sight will prove to be sufficient in our analyses. In what follows, we will explore the formation and evolution of several instability modes including axisymmetric and non-axisymmetric patterns through the established model (23).

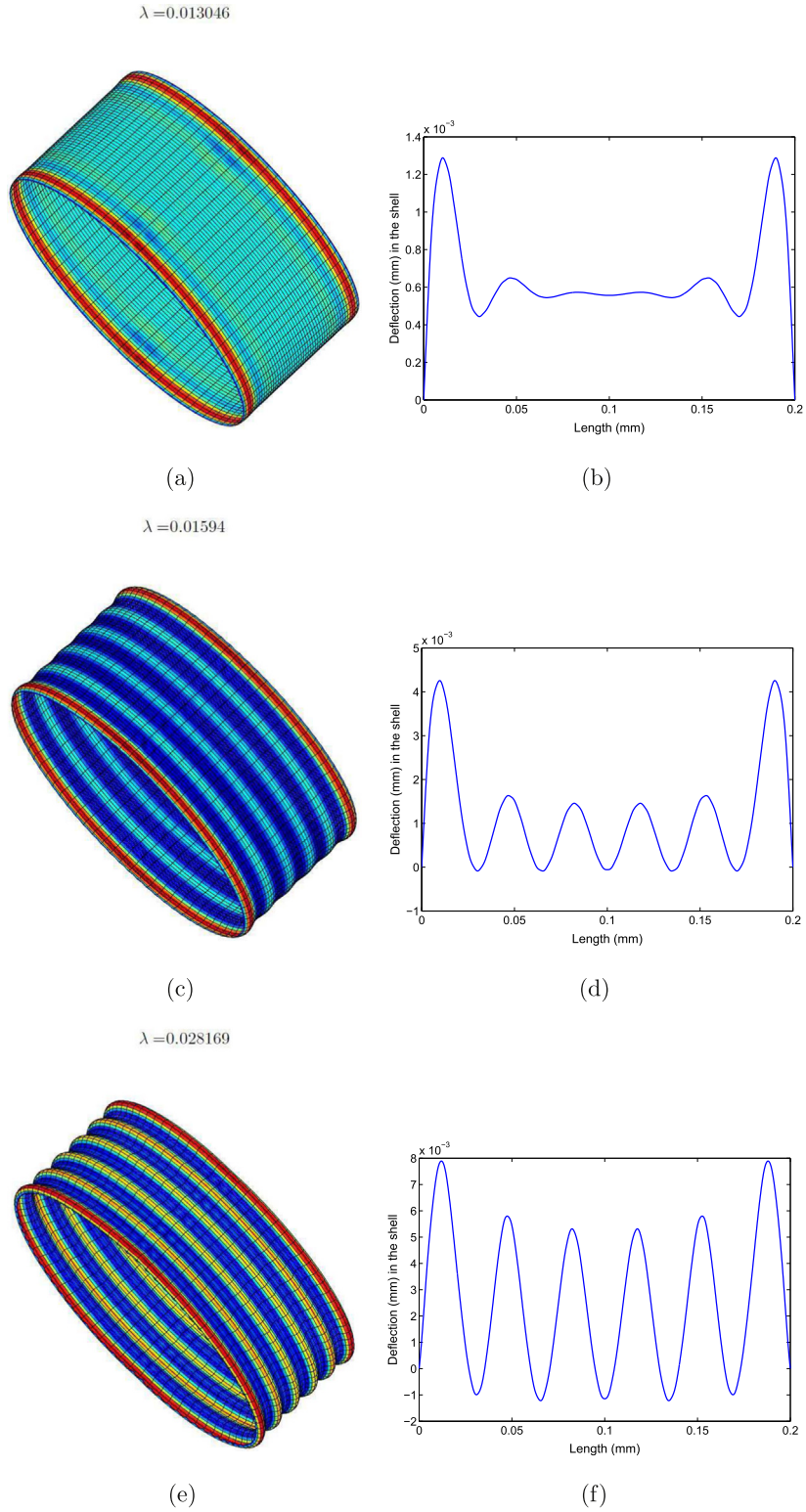
### 5.1. Axisymmetric sinusoidal pattern

First, we investigate the pattern formation and evolution via Core-shell I with  $E_f/E_s = 722$  and  $R/h_f = 200$  that corresponds to  $C_s = 3.92$ . The shell is uniaxially compressed along the  $x$  direction as shown in Fig. 5. At the two ends of the core-shell cylinder, the radial displacements  $v_2$ ,  $v_3$ ,  $w_2$  and  $w_3$  are locked. To avoid rigid body motions, the axial displacement  $v_1$  in the shell center is locked as well. Due to the geometric symmetry, only one quarter of the system can be considered for the mesh and symmetry conditions on the edges are suitably applied. Consequently, the surface layer is meshed with  $20 \times 50$  shell elements to ensure at least five elements within a single wave. The core is compatibly discretized by 5000 brick elements with five layers. The relevant discussion of this mesh is provided in Supplementary material. Totally, the core-shell system contains 41,337 degrees of freedom (DOF) including the Lagrange multipliers.

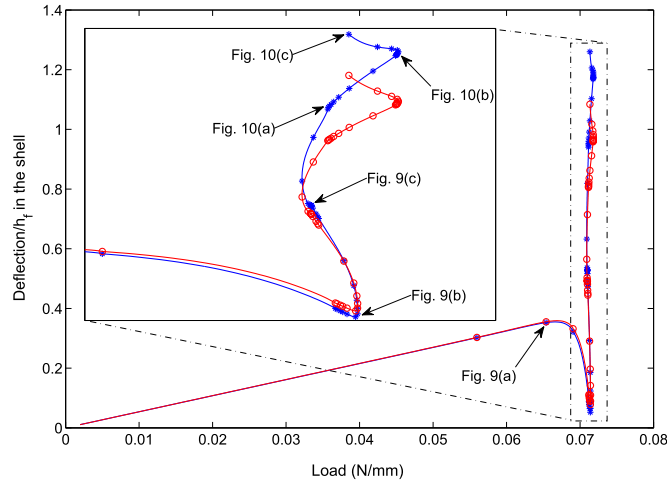
The critical load of axisymmetric sinusoidal wrinkles based on the linearized stability analysis of Donnell–Muskhvishvili (DMV) shell equations was provided (Karam and Gibson, 1995; Zhao et al., 2014), with linear elasticity assumption for the material. The critical load can be expressed as  $\sigma_{cr} = E_f [1/p_0^2 + h_f^2 p_0^2 / (4c^2 R^2) + 3RE_s / (2c^2 h_f E_f p_0)]$ , where  $\bar{E}_f = E_f / (1 - \nu_f^2)$ ,  $\bar{E}_s = E_s / (1 - \nu_s^2)$  and  $c = \sqrt{3(1 - \nu_f^2)}$ . The critical wave number along the axial direction,  $p_0$ , is determined by solving the equation  $-2 + h_f^2 p_0^4 / (2c^2 R^2) - 3RE_s p_0 / (2c^2 h_f \bar{E}_f) = 0$ . By introducing the material and geometric parameters of Core-shell I in Table 1, one can obtain the analytical solution of compressive force in the shell  $F_{cr} = \sigma_{cr} h_f = 0.012$  N/mm, which is close to our 3D finite element results (about 0.013 N/mm in Fig. 6).

The established 3D model based on the ANM offers a very fast computing speed to reach the critical point with only three steps (see Fig. 6), with an adaptive reduction of step length. A sequence of representative wrinkling patterns on the load-displacement curve is illustrated in Fig. 7. A wrinkling mode with boundary effects firstly occurs at the ends of the core-shell system as shown in Fig. 7a and b, which corresponds to the regions where compressive stresses are larger. When the load increases to the second bifurcation, an axisymmetric sinusoidal mode emerges and grows (see Fig. 7c and d). In the end, boundary effects tend to be not so obvious and a uniformly distributed axisymmetric mode matures (see Fig. 7e and f). As for the axisymmetric mode, the post-bifurcation curve in Fig. 6 is constantly supercritical. Other calculations with various values of  $C_s$  greater than 0.9 have been achieved and the bifurcation portrait is always the same. At the first bifurcation, the buckling mode is axisymmetric and localized in boundary layers. This boundary effect is also well known in pure shell structures and it can be clearly predicted by Eq. (12), but in the latter case the deformed shape quickly becomes non-axisymmetric, which has not been observed in core-shell cylinders with  $C_s \geq 0.9$ . Moreover, a stable post-bifurcation response has been found in all these cases, which is typical of the core-shell cylinders with  $C_s \geq 0.9$  and has never been observed in pure cylindrical shells whose post-buckling behavior is highly unstable and imperfection-sensitive.

Therefore, a generic response emerges for any core-shell cylindrical system with a sufficiently stiff core ( $C_s \geq 0.9$ ): a



**Fig. 7.** The left column shows a sequence of representative wrinkling patterns of Core-shell I with  $C_s = 3.92$  under axial compression. The right column presents the associated instability modes along the length.



**Fig. 8.** Bifurcation curves of Core-shell II with  $C_s=0.43$  under axial compression: the points A and B are depicted by blue and red colors, respectively. Representative wrinkling shapes in Figs. 9 and 10 on the post-buckling evolution path are marked. ANM parameters:  $n=15$ ,  $\delta=10^{-3}$ , 50 steps. Each point corresponds to one ANM step. (For interpretation of the references to color in this figure caption, the reader is referred to the web version of this paper.)

stable post-bifurcation and an axisymmetric buckled shape that is localized in boundary layers at the beginning and then tends to be more uniformly distributed sinusoidal pattern. The existence of this stable post-buckling response was explored in Zhao et al. (2014) theoretically and experimentally, but without mentioning a single dimensionless parameter.

## 5.2. Non-axisymmetric diamond-like pattern

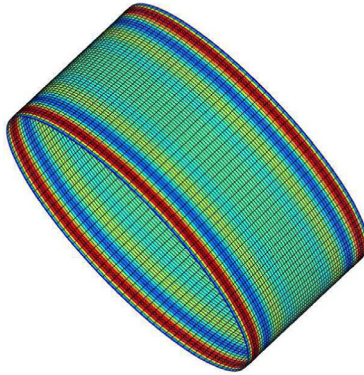
Three-dimensional spatial wrinkling modes are then explored via Core-shell II with a larger  $E_f/E_s = 12,000$  and  $R/h_f = 300$  that is equivalent to  $C_s=0.43$ . One quarter of the system is also taken into account for the calculation due to the symmetry. The loading and boundary conditions are kept to be the same as before. One quarter of the surface is meshed with  $30 \times 60$  shell elements and the core is compatibly discretized by 9000 brick elements with five layers. Totally, the core-shell system contains 73,197 DOF including the Lagrange multipliers.

The ANM takes very big step lengths to reach the critical load, then the step length automatically shortens around the bifurcation (see Fig. 8). Figs. 9 and 10 present a sequence of representative wrinkling patterns on the post-buckling response curves in Fig. 8 where five bifurcations have been observed. The first two instability modes show an evolution of sinusoidally deformed axisymmetric shape with boundary effects at the beginning (see Fig. 9a and b), which indicates that the critical buckling mode is axisymmetric and independent of the modulus ratio of the surface layer to the core. These two bifurcations appear to be supercritical. When the load reaches the third bifurcation that is slightly subcritical, non-axisymmetric diamond shaped patterns occur (see Fig. 9c) and grow at the fourth and fifth bifurcations (see Fig. 10a and b). This demonstrates that the axisymmetric mode evolves into a non-axisymmetric diamond-like shape at the third bifurcation, if the modulus ratio is larger than a critical value. This critical modulus ratio was drawn as a function of radius ratio  $R/h_f$  by Zhao et al. (2014) and our two numerical cases are well located in their corresponding regions of the phase diagram determined by the dimensionless parameter  $C_s$  (see Fig. 2). From the fifth bifurcation, two neighboring diamond shaped patterns begin to merge into a bigger one near the boundary and this matures in the final step as shown in Fig. 10c. A localization mode in the form of alternating deep and shallow diamond-like shapes in the circumferential direction appear in the bulk of the shell.

Next we study Core-shell III that has a quite small critical value  $C_s=0.1$ . The symmetry, mesh, DOF, loading and boundary conditions are exactly the same as in the last case. The load-displacement curve turns out to be quite subcritical after the first bifurcation where a boundary mode appears (see Figs. 11 and 12b). The diamond shaped pattern emerges after the first bifurcation and matures at the second bifurcation (see Fig. 12c). A localization in the form of alternating deep and shallow diamond-like shapes in the circumferential direction is also observed near the ends of the system and it actively evolves along the circumferential direction with respect to the loading (compare Fig. 12c and e). We can further consider Core-shell IV that holds an extremely small critical value  $C_s=0.01$  and a huge modulus ratio  $E_f/E_s = 120,000$ . The load-displacement response in Fig. 13 suggests that the strongly subcritical post-buckling behavior where the load reduces 70% of its maximum value is rather similar to the buckling of classical cylindrical shell without a core where the load can decline up to 80%. This is reasonable since the huge modulus ratio in the core-shell cylinder approximates to a pure cylindrical shell. The associated instability mode shows a very localized diamond shaped pattern near the ends (see Supplementary material). Nevertheless, the importance of the deformed shape should not be overestimated since Core-shell IV is close to a pure shell where there exist many solutions that are very imperfection-sensitive.

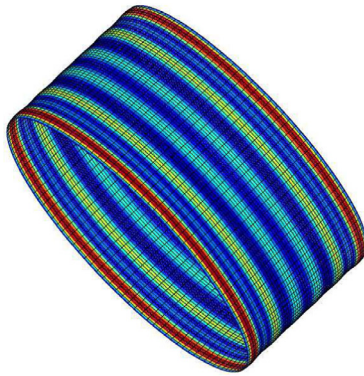
Therefore, another type of generic response has been observed in the case of a soft core ( $C_s \leq 0.7$ ). Typically, the pattern is diamond shaped and the post-bifurcation response is unstable. The softer the core is, the more subcritical the post-buckling

$$\lambda = 0.065375$$



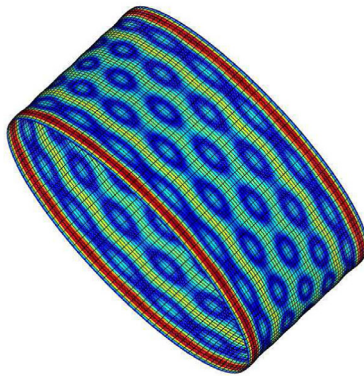
(a)

$$\lambda = 0.071402$$



(b)

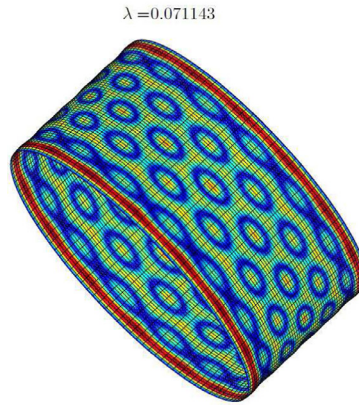
$$\lambda = 0.070989$$



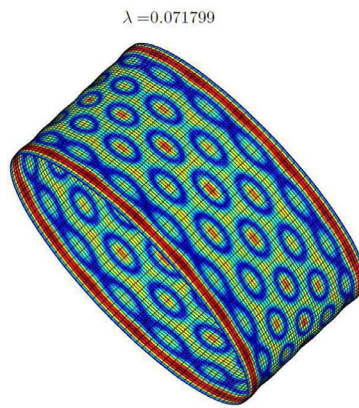
(c)

**Fig. 9.** A sequence of representative wrinkling patterns of Core-shell II with  $C_s=0.43$  at the initial post-buckling stage.

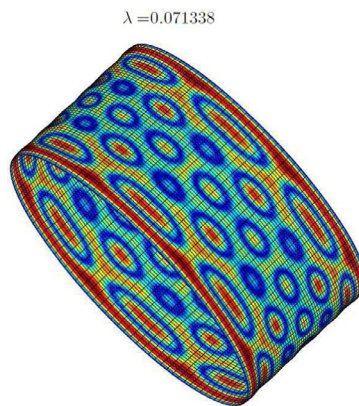




(a)

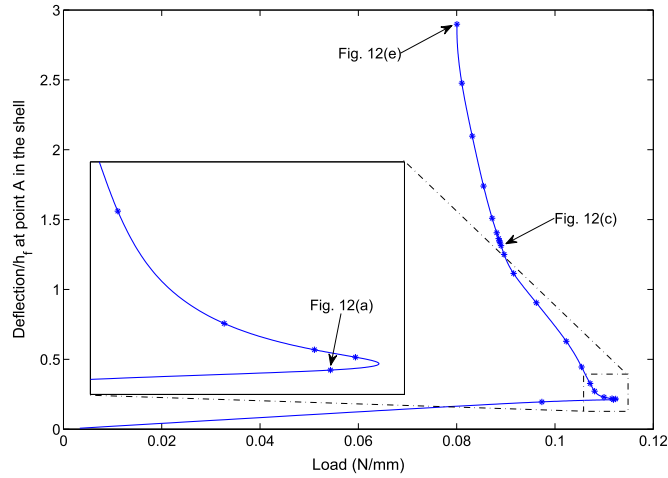


(b)



(c)

**Fig. 10.** A sequence of representative wrinkling patterns of Core-shell II with  $C_s=0.43$  at the final post-buckling stage.



**Fig. 11.** Bifurcation curve of Core-shell III with  $C_s=0.1$  under axial compression. Representative wrinkling shapes in Fig. 12 on the post-buckling evolution path are marked. ANM parameters:  $n=15$ ,  $\delta=10^{-3}$ , 22 steps. Each point corresponds to one ANM step.

behavior is and therefore the structure is highly imperfection-sensitive. For an extremely soft core ( $C_s \leq 0.01$ ), the minimal load in the bifurcation diagram is very small and corresponds to a reduction of 70–80% with respect to the first bifurcation. These non-axisymmetric diamond-like modes emerge after the secondary bifurcation, the first bifurcation remaining axisymmetric and localized near the boundary. This second class of post-buckling response looks like the well known post-buckling behavior of a pure shell and the existence of two typical post-buckling schemes is in agreement with the theoretical and experimental results in Zhao et al. (2014).

### 5.3. Last discussions

The existence of two basic schemes and the major influence of the dimensionless parameter  $C_s$  have been established numerically. It is natural to compare this statement with recent experimental results reported in Zhao et al. (2014). A representative comparison is given in Fig. 14 and a larger collection of such qualitative comparisons can be found in Supplementary information. Clearly the experimental observations confirm the existence of two classes of structural responses that are determined by the parameter  $C_s$ .

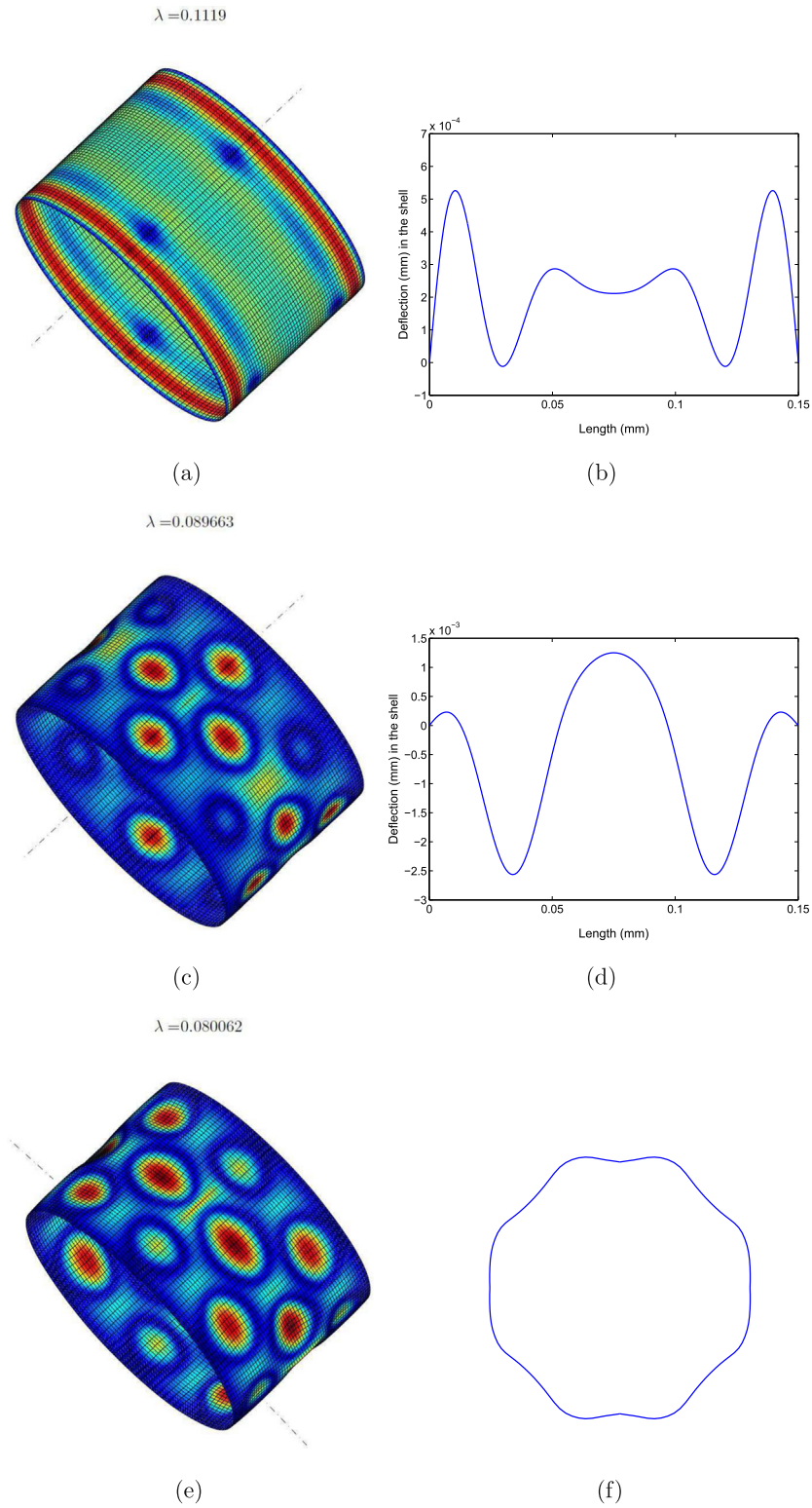
To what extent such schemes remain valid in other cases of geometry, loading and boundary conditions? The behavior of non-cylindrical core-shells has been recently investigated in Stoop et al. (2015) by modeling the film based on the famous Koiter's shell equations (Koiter, 1966; Ciarlet, 2000) that is often considered as the best shell theory. Let us consider a shell with two principal curvatures being of the order of  $R$  in the initial configuration. In many cases as the axially compressed cylinders studied here or the pressurized spherical shell analyzed in Stoop et al. (2015), the buckling wavelength  $\ell$  is usually small with respect to the structural length  $R$ . In other words, the deformed geometry is assumed to be much more wavy than the initial one. With this assumption, the dimensional analysis in Section 2.3 can be easily extended to any shell geometry by starting from the same dimensionless parameters presented in Eq. (13). The key points are the expressions of the membrane strain and the curvature change (see for instance in Stoop et al. (2015), supplementary information, Eqs. (16) and (18)):

$$\gamma_{\alpha\beta} = \frac{1}{2}(\mathbf{u}_{\alpha,\beta} + \mathbf{u}_{\beta,\alpha} + \mathbf{u}_{\gamma,\alpha}\mathbf{u}_{\gamma,\beta} + \mathbf{w}_{,\alpha}\mathbf{w}_{,\beta}) - \Gamma_{\alpha\beta}^{\sigma}\mathbf{u}_{\sigma} - b_{\alpha\beta}\mathbf{w}, \quad (28)$$

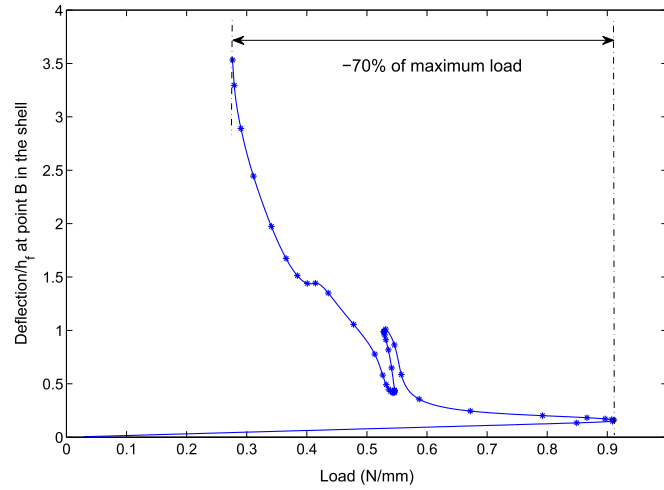
$$K_{\alpha\beta} = (\mathbf{u}_{,\alpha\beta} - \Gamma_{\alpha\beta}^{\sigma}\mathbf{u}_{,\sigma}) \cdot \mathbf{n}, \quad (29)$$

where  $\Gamma_{\alpha\beta}^{\sigma}$  is the Christoffel symbol,  $b_{\alpha\beta}$  denotes the initial curvature tensor and  $\mathbf{n}$  represents the initial normal vector. Obviously  $\Gamma_{\alpha\beta}^{\sigma}$  and  $b_{\alpha\beta}$  are of the order of  $1/R$ . Greek indices  $\alpha, \beta, \dots$  take values in  $\{1, 2\}$ . From the order of magnitude (13), the membrane strain is of the order of  $h_f/R = h_f^2/\ell^2$ , which is due to the quantities  $(\mathbf{w}_{,\alpha}\mathbf{w}_{,\beta}/2 - b_{\alpha\beta}\mathbf{w})$  in Eq. (28), the other terms in Eq. (28) being smaller. In the same way, the curvature  $K_{\alpha\beta}$  of the deformed shell is apparently of the order of  $h_f/\ell^2$ . This leads to the same orders of magnitude as in Eq. (16) so that the analyses in Section 2.3 have been extended to any core-shell buckling problem where the instability wavelength is of the order of  $\sqrt{Rh_f}$ . Therefore, the dimensionless parameter  $C_s$  governs the response of various core-shell buckling problems, for instance the surface wrinkling of core-shell spheres. In the case of a cylinder under external pressure or torsion (Yamaki, 1984; Abdelmoula and Leger, 2008), the buckling mode shapes are different so that a consistent dimensional analysis would lead to other dimensionless parameters.

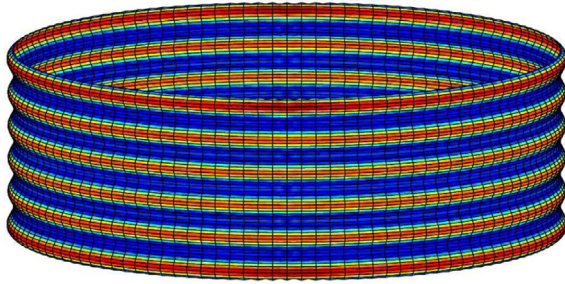




**Fig. 12.** The left column shows a sequence of representative wrinkling patterns of Core-shell III with  $C_s=0.1$  under axial compression. The right column presents the associated instability modes.



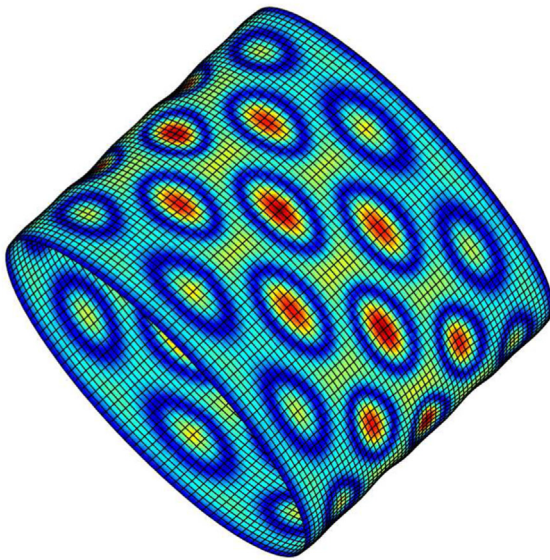
**Fig. 13.** Bifurcation curve of Core-shell IV with  $C_s=0.01$  under axial compression. The extremely subcritical load–displacement diagram suggests that the load can decrease 70% of its maximum value. ANM parameters:  $n=15$ ,  $\delta=10^{-3}$ , 46 steps. Each point corresponds to one ANM step.



(a)



(b)



(c)



(d)

**Fig. 14.** Comparison of two representative instability patterns (axisymmetric sinusoidal and non-axisymmetric diamond-like) between our numerical results (left column) and the experiments (right column) in Zhao et al. (2014): (a) and (b) show axisymmetric modes, with  $C_s=2$ ,  $R/h_f=400$  and  $E_f/E_s=4000$ ; (c) and (d) present non-axisymmetric diamond shaped modes, with  $C_s=0.33$ ,  $R/h_f=120$  and  $E_f/E_s=4000$ . More cases are reported in Supplementary material.

## 6. Concluding remarks

Pattern formation and post-buckling evolution of core–shell soft cylindrical systems were investigated theoretically and numerically from a quantitative standpoint. The critical parameter  $C_s$  that determines post-buckling pattern selection has been found qualitatively through dimensional analysis of Donnell–Mushtari–Vlassov (DMV) and Koiter's shell equations. The further quantitative investigation is performed numerically based on a 3D finite element model associating geometrically nonlinear shell formulation for the surface layer and linear elasticity for the core. This core–shell model can describe moderately large rotations and displacements on the surface. The presented results rely heavily on robust resolution techniques based on the ANM that is able to detect multiple bifurcations on a severely nonlinear response curve and to trace the whole post-buckling evolution on the equilibrium path. We have been able to compute some extreme cases with a huge modulus ratio (e.g.  $E_f/E_s = 120,000$ ) or a large radius/thickness ratio (e.g.  $R/h_f \approx 500$ ), which really requires a robust path-following technique and an efficient locking-free shell model. The occurrence and evolution of sinusoidally deformed axisymmetric patterns and non-axisymmetric diamond-like modes have been observed in the post-buckling range.

As for planar film/substrate systems, uniaxial compression generally leads to 1D sinusoidal surface wrinkles perpendicular to the loading direction (Xu et al., 2014, 2015a; Xu and Potier-Ferry, 2016). As for the present core–shell cylindrical structures under uniaxial compression, buckling and post-buckling behavior mainly depends on the core stiffness measured by the dimensionless parameter  $C_s = (E_s/E_f)(R/h_f)^{3/2}$ . Precisely, for a stiff core ( $C_s \geq 0.9$ ), the buckling pattern is axisymmetric and post-bifurcation solutions are stable; whereas for a soft core ( $C_s \leq 0.7$ ), the bifurcated solution branch is often subcritical and the associated instability modes are diamond shaped after secondary bifurcations. Furthermore, for a very soft core ( $C_s \leq 0.01$ ), the behavior turns out to be close to pure shells which are well known to be highly unstable and imperfection-sensitive. In any case, the pattern around the first bifurcation is axisymmetric and localized near the boundary, as in the case of pure shell structures. These two bifurcation schemes seem to be generic for a perfect core–shell cylinder subjected to axial compression and have been observed in any case, except in the narrow transition zone ( $0.7 < C_s < 0.9$ ) where the mode may switch from one scenario to the other. Indeed, other instability modes and bifurcation schemes would be obtained under different geometries and loading conditions, as known for pure shells. The relevance of this parameter  $C_s$  has been established from the dimensional analysis for core–shell cylindrical systems governed by the DMV and Koiter's shell equations for the surface and 3D linear elasticity for the core, and it seems to well hold for many core–shell problems with a wavy buckling mode. Two other dimensionless parameters also exist in the system. Nevertheless, like the famous Batdorf parameter, they mostly affect the wave number and boundary mode around the first bifurcation.

## Acknowledgments

F. Xu acknowledges the start-up funds from Fudan University. The authors are also grateful for the financial support from French National Research Agency ANR (LabEx DAMAS, Grant no. ANR-11-LABX-0008-01).

## Appendix A. Shell formulations

In the initial undeformed configuration, the position vector  $\mathbf{x}$  representing any point in the shell can be defined as

$$\mathbf{x}(\theta^\alpha, \theta^3) = \mathbf{r}(\theta^\alpha) + \theta^3 \mathbf{a}_3(\theta^\alpha), \quad (30)$$

where  $\mathbf{r}(\theta^\alpha)$  ( $\alpha = 1, 2$ ) denotes the projection of  $\mathbf{x}$  in the middle surface and  $\theta^3$  describes its perpendicular direction with  $\theta^3 \in [-h_f/2, h_f/2]$  in which  $h_f$  is the reference thickness of shell. The normal vector of middle surface is represented by  $\mathbf{a}_3 = \mathbf{a}_1 \times \mathbf{a}_2$ .

Similarly, in the current deformed configuration, we define the position of point  $\mathbf{x}$  by the vector  $\bar{\mathbf{x}}$ :

$$\bar{\mathbf{x}}(\theta^\alpha, \theta^3) = \bar{\mathbf{r}}(\theta^\alpha) + \theta^3 \bar{\mathbf{a}}_3(\theta^\alpha), \quad (31)$$

where

$$\begin{cases} \bar{\mathbf{r}} = \mathbf{r} + \mathbf{v}, \\ \bar{\mathbf{a}}_3 = \mathbf{a}_3 + \mathbf{w}. \end{cases} \quad (32)$$

Therefore, the displacement vector associated with an arbitrary material point in the shell, linearly varies along the thickness direction reads

$$\mathbf{u}(\theta^\alpha, \theta^3) = \bar{\mathbf{x}} - \mathbf{x} = \mathbf{v}(\theta^\alpha) + \theta^3 \mathbf{w}(\theta^\alpha). \quad (33)$$

Totally, six degrees of freedom can be distinguished in Eq. (33) to describe the shell kinematics: three vector components related to the translation of the middle surface ( $v_1, v_2, v_3$ ) and other three components updating the direction vector ( $w_1, w_2, w_3$ ).

The Green–Lagrange strain tensor is used to describe geometric nonlinearity, which can be expressed in the covariant

base:

$$\boldsymbol{\gamma} = \frac{1}{2}(\bar{\mathbf{g}}_{ij} - \mathbf{g}_{ij})\mathbf{g}^i \otimes \mathbf{g}^j \quad \text{with } i, j = 1, 2, 3, \quad (34)$$

where  $\mathbf{g}^i$  are the contravariant base vectors, while  $\mathbf{g}_{ij} = \mathbf{g}^i \cdot \mathbf{g}^j$  and  $\bar{\mathbf{g}}_{ij} = \bar{\mathbf{g}}^i \cdot \bar{\mathbf{g}}^j$  respectively represent the components of covariant metric tensor in the initial configuration and the deformed one (Büchter et al., 1994).

Concerning the enhanced assumed strain  $\tilde{\boldsymbol{\gamma}}$ , classical shell kinematics requires the transversal strain field to be zero ( $\gamma_{33} = 0$ ). In reality, since 3D constitutive relations are concerned, this condition is hardly satisfied due to Poisson effect, especially for bending dominated cases. This phenomenon is commonly referred to as “Poisson thickness locking”. To remedy this issue, an enhanced assumed strain  $\tilde{\boldsymbol{\gamma}}$  contribution has been introduced in the shell formulation (Büchter et al., 1994), acting across the shell thickness direction and supplementing the compatible strain field  $\boldsymbol{\gamma}_\mu$ . It describes the linear variation of the thickness stretch or compression, and is expressed with respect to the local curvilinear coordinates  $\theta^3$ :

$$\tilde{\boldsymbol{\gamma}} = \theta^3 \tilde{\gamma}_{33} \mathbf{g}^3 \otimes \mathbf{g}^3 \quad \text{with } \tilde{\gamma}_{33} = \tilde{\gamma}_{33}(\theta^3), \quad (35)$$

and satisfies the condition of orthogonality with respect to the stress field  $\mathbf{S}$ :

$$\int_{\Omega_f} {}^t\mathbf{S} : \tilde{\boldsymbol{\gamma}} \, d\Omega = 0. \quad (36)$$

In this way, “spurious” transversal strains induced by Poisson effect for bending dominated kinematics are balanced by the assumed strain  $\tilde{\boldsymbol{\gamma}}$ , which clears the “thickness locking” problem. This approach is applied in this paper, since the associated finite element is very efficient, especially for very thin shells (Zahrouni et al., 1999; Boutyour et al., 2004).

## Appendix B. Supplementary data

Supplementary data associated with this paper can be found in the online version at <http://dx.doi.org/10.1016/j.jmps.2016.04.025>.

## References

- Abdelmoula, R., Damil, N., Potier-Ferry, M., 1992. Influence of distributed and localized imperfections on the buckling of cylindrical shells under external pressure. *Int. J. Solids Struct.* 29, 1–25.
- Abdelmoula, R., Leger, A., 2008. Singular perturbation analysis of the buckling of circular cylindrical shells. *Eur. J. Mech. A—Solids* 27, 706–729.
- Allen, H.G., 1969. *Analysis and Design of Structural Sandwich Panels*. Pergamon Press, New York.
- Allgower, E.L., Georg, K., 1990. *Numerical Continuation Methods*. Springer-Verlag, Berlin.
- Arbocz, J., 1987. Post-buckling behaviour of structures numerical techniques for more complicated structures. In: *Buckling and Post-Buckling: Lecture Notes in Physics*, vol. 288, Springer-Verlag, Heidelberg, pp. 83–142.
- Audoly, B., Boudaoud, A., 2008. Buckling of a stiff film bound to a compliant substrate—Part I: formulation, linear stability of cylindrical patterns, secondary bifurcations. *J. Mech. Phys. Solids* 56, 2401–2421.
- Baguet, S., Cochelin, B., 2003. On the behaviour of the ANM continuation in the presence of bifurcations. *Commun. Numer. Methods Eng.* 19, 459–471.
- Biot, M.A., 1937. Bending of an infinite beam on an elastic foundation. *J. Appl. Mech.* 203, A1–A7.
- Boutyour, E.H., Zahrouni, H., Potier-Ferry, M., Boudi, M., 2004. Bifurcation points and bifurcated branches by an asymptotic numerical method and Padé approximants. *Int. J. Numer. Methods Eng.* 60, 1987–2012.
- Bowden, N., Brittain, S., Evans, A.G., Hutchinson, J.W., Whitesides, G.M., 1998. Spontaneous formation of ordered structures in thin films of metals supported on an elastomeric polymer. *Nature* 393, 146–149.
- Brau, F., Vandeparre, H., Sabbah, A., Poulard, C., Boudaoud, A., Damman, P., 2011. Multiple-length-scale elastic instability mimics parametric resonance of nonlinear oscillators. *Nat. Phys.* 7, 56–60.
- Breid, D., Crosby, A.J., 2013. Curvature-controlled wrinkle morphologies. *Soft Matter* 9, 3624–3630.
- Büchter, N., Ramm, E., Roehl, D., 1994. Three-dimensional extension of non-linear shell formulation based on the enhanced assumed strain concept. *Int. J. Numer. Methods Eng.* 37, 2551–2568.
- Bushnell, D., 1985. *Computerized Buckling Analysis of Shells*. Kluwer Academic Publishers, Dordrecht.
- Bushnell, D., Bushnell, B., 2015. *Shell Buckling*. (<http://shellbuckling.com>).
- Cai, Z., Fu, Y., 2000. Exact and asymptotic stability analyses of a coated elastic half-space. *Int. J. Solids Struct.* 37, 3101–3119.
- Cao, Y., Hutchinson, J.W., 2012. Wrinkling phenomena in neo-Hookean film/substrate bilayers. *J. Appl. Mech.* 79, 031019-1–031019-9.
- Chan, E.P., Crosby, A.J., 2006. Fabricating microlens arrays by surface wrinkling. *Adv. Mater.* 18, 3238–3242.
- Chen, X., Hutchinson, J.W., 2004. Herringbone buckling patterns of compressed thin films on compliant substrates. *J. Appl. Mech.* 71, 597–603.
- Chen, X., Yin, J., 2010. Buckling patterns of thin films on curved compliant substrates with applications to morphogenesis and three-dimensional micro-fabrication. *Soft Matter* 6, 5667–5680.
- Ciarlet, P.G., 2000. *Mathematical Elasticity: Theory of Shells*, vol. 3. North Holland, Amsterdam.
- Cochelin, B., 1994. A path-following technique via an asymptotic-numerical method. *Comput. Struct.* 53, 1181–1192.
- Cochelin, B., Damil, N., Potier-Ferry, M., 1994. Asymptotic-numerical Methods and Padé approximants for non-linear elastic structures. *Int. J. Numer. Methods Eng.* 37, 1187–1213.
- Cochelin, B., Damil, N., Potier-Ferry, M., 2007. *Méthode Asymptotique Numérique*. Hermès Science Publications, Paris.
- Cochelin, B., Medale, M., 2013. Power series analysis as a major breakthrough to improve the efficiency of Asymptotic Numerical Method in the vicinity of bifurcations. *J. Comput. Phys.* 236, 594–607.
- Damil, N., Potier-Ferry, M., 1990. A new method to compute perturbed bifurcation: application to the buckling of imperfect elastic structures. *Int. J. Eng. Sci.* 26, 943–957.



- Doedel, E., 1981. AUTO: a program for the automatic bifurcation analysis of autonomous systems. *Congr. Numer.* 30, 265–284.
- Efimenko, K., Rackaitis, M., Manias, E., Vaziri, A., Mahadevan, L., Genzer, J., 2005. Nested self-similar wrinkling patterns in skins. *Nat. Mater.* 4, 293–297.
- Howarter, J.A., Stafford, C.M., 2010. Instabilities as a measurement tool for soft materials. *Soft Matter* 6, 5661–5666.
- Huang, Z.Y., Hong, W., Suo, Z., 2005. Nonlinear analyses of wrinkles in a film bonded to a compliant substrate. *J. Mech. Phys. Solids* 53, 2101–2118.
- Hutchinson, J.W., Koiter, W.T., 1970. Postbuckling theory. *Appl. Mech. Rev.* 23, 1353–1366.
- Jia, F., Li, B., Cao, Y., Xie, W., Feng, X., 2015. Wrinkling pattern evolution of cylindrical biological tissues with differential growth. *Phys. Rev. E* 91, 012403–1–012403–8.
- Julien, J.F., 1991. *Buckling of Shell Structures, on Land, in the Sea and in the Air*. Taylor & Francis, London.
- Karam, G.N., Gibson, L.J., 1995. Elastic buckling of cylindrical shells with elastic cores—I. Analysis. *Int. J. Solids Struct.* 32, 1259–1283.
- Koiter, W.T., 1945. *On the Stability of Elastic Equilibrium* (Thesis). Delft, H.J. Paris, Amsterdam. An English translation is available from: (<http://imechanica.org/node/14005>) (in Dutch with English summary).
- Koiter, W.T., 1966. On the nonlinear theory of thin elastic shells. *Proc. K. Ned. Akad. Wet. B* 69, 1–54.
- Koiter, W.T., 2009. W.T. Koiter's elastic stability of solids and structures. In: van der Heijden, A.M.A. (Ed.), . Cambridge University Press, Cambridge.
- Li, B., Jia, F., Cao, Y.P., Feng, X.Q., Gao, H., 2011. Surface wrinkling patterns on a core-shell soft sphere. *Phys. Rev. Lett.* 106, 234301–1–234301–4.
- Mahadevan, L., Rica, S., 2005. Self-organized origami. *Science* 307, 1740.
- Medale, M., Cochelin, B., 2009. A parallel computer implementation of the Asymptotic Numerical Method to study thermal convection instabilities. *J. Comput. Phys.* 228, 8249–8262.
- Myint-U, T., 1969. Post-buckling behavior of axially compressed core-filled cylinders. *Z. Angew. Math. Mech.* 49, 423–426.
- Rogers, J.A., Someya, T., Huang, Y., 2010. Materials and mechanics for stretchable electronics. *Science* 327, 1603–1607.
- Shield, T.W., Kim, K.S., Shield, R.T., 1994. The buckling of an elastic layer bonded to an elastic substrate in plane strain. *J. Appl. Mech.* 61, 231–235.
- Simo, J.C., Rifai, M.S., 1990. A class of mixed assumed strain methods and method of incompatible modes. *Int. J. Numer. Methods Eng.* 37, 1595–1636.
- Song, J., Jiang, H., Liu, Z.J., Khang, D.Y., Huang, Y., Rogers, J.A., Lu, C., Koh, C.G., 2008. Buckling of a stiff thin film on a compliant substrate in large deformation. *Int. J. Solids Struct.* 45, 3107–3121.
- Steigmann, D., Ogden, R.W., 1997. Plane deformations of elastic solids with intrinsic boundary elasticity. *Proc. R. Soc. A* 453, 853–877.
- Stoop, N., Lagrange, R., Terwagne, D., Reis, P.M., Dunkel, J., 2015. Curvature-induced symmetry breaking determines elastic surface patterns. *Nat. Mater.* 14, 337–342.
- Sun, J.Y., Xia, S., Moon, M.W., Oh, K.H., Kim, K.S., 2012. Folding wrinkles of a thin stiff layer on a soft substrate. *Proc. R. Soc. A* 468, 932–953.
- Teng, J.G., 1996. Buckling of thin shells: recent advances and trends. *Appl. Mech. Rev.* 49, 263–274.
- Teng, J.G., Rotter, J.M., 2006. *Buckling of Thin Metal Shells*. Taylor & Francis, London.
- Terwagne, D., Brojan, M., Reis, P.M., 2014. Smart morphable surfaces for aerodynamic drag control. *Adv. Mater.* 26, 6608–6611.
- Vannucci, P., Cochelin, B., Damil, N., Potier-Ferry, M., 1998. An asymptotic-numerical method to compute bifurcating branches. *Int. J. Numer. Methods Eng.* 41, 1365–1389.
- von Kármán, Th., Tsien, H.S., 1941. The buckling of thin cylindrical shells under axial compression. *J. Aeronautical Sci.* 8, 303–312.
- Wu, J., Cheng, Q.H., Liu, B., Zhang, Y.W., Lu, W.B., Hwang, K.C., 2012. Study on the axial compression buckling behaviors of concentric multi-walled cylindrical shells filled with soft materials. *J. Mech. Phys. Solids* 60, 803–826.
- Xu, F., 2014. *Numerical Study of Instability Patterns of Film-Substrate Systems* (Ph.D. thesis). Université de Lorraine, France.
- Xu, F., Koutsawa, Y., Potier-Ferry, M., Belouettar, S., 2015a. Instabilities in thin films on hyperelastic substrates by 3D finite elements. *Int. J. Solids Struct.* 69–70, 71–85.
- Xu, F., Potier-Ferry, M., 2016. A multi-scale modeling framework for instabilities of film/substrate systems. *J. Mech. Phys. Solids* 86, 150–172.
- Xu, F., Potier-Ferry, M., Belouettar, S., Cong, Y., 2014. 3D finite element modeling for instabilities in thin films on soft substrates. *Int. J. Solids Struct.* 51, 3619–3632.
- Xu, F., Potier-Ferry, M., Belouettar, S., Hu, H., 2015b. Multiple bifurcations in wrinkling analysis of thin films on compliant substrates. *Int. J. Nonlinear Mech.* 76, 203–222.
- Yamaki, N., 1984. *Elastic Stability of Circular Cylindrical Shells*. North-Holland, Amsterdam.
- Yao, J.C., 1962. Buckling of axially compressed long cylindrical shell with elastic core. *J. Appl. Mech.* 29, 329–334.
- Ye, L., Lu, G., Ong, L.S., 2011. Buckling of a thin-walled cylindrical shell with foam core under axial compression. *Thin Wall. Struct.* 49, 106–111.
- Yin, J., Chen, X., Sheinman, I., 2009. Anisotropic buckling patterns in spheroidal film/substrate systems and their implications in some natural and biological systems. *J. Mech. Phys. Solids* 57, 1470–1484.
- Zahrouni, H., Cochelin, B., Potier-Ferry, M., 1999. Computing finite rotations of shells by an asymptotic-numerical method. *Comput. Methods Appl. Mech. Eng.* 175, 71–85.
- Zang, J., Zhao, X., Cao, Y., Hutchinson, J.W., 2012. Localized ridge wrinkling of stiff films on compliant substrates. *J. Mech. Phys. Solids* 60, 1265–1279.
- Zhao, Y., Cao, Y., Feng, X., Ma, K., 2014. Axial compression-induced wrinkles on a core-shell soft cylinder: theoretical analysis, simulations and experiments. *J. Mech. Phys. Solids* 73, 212–227.

## Supplementary Information

Very fine meshes, at least five or ten elements within a single wavelength, are adopted to discretize the core-shell cylinders in both circumferential and axial directions. As for the radial direction, a convergence analysis is examined through the test with different discretizations of layers in the core, *i.e.* 5, 10, 12 and 15 layers, respectively. From Fig. S1, it can be observed that all the post-buckling bifurcation curves share the same trend and quite close bifurcation points, which suggests that the numerical results are converged and the post-buckling modes should be very similar among them.

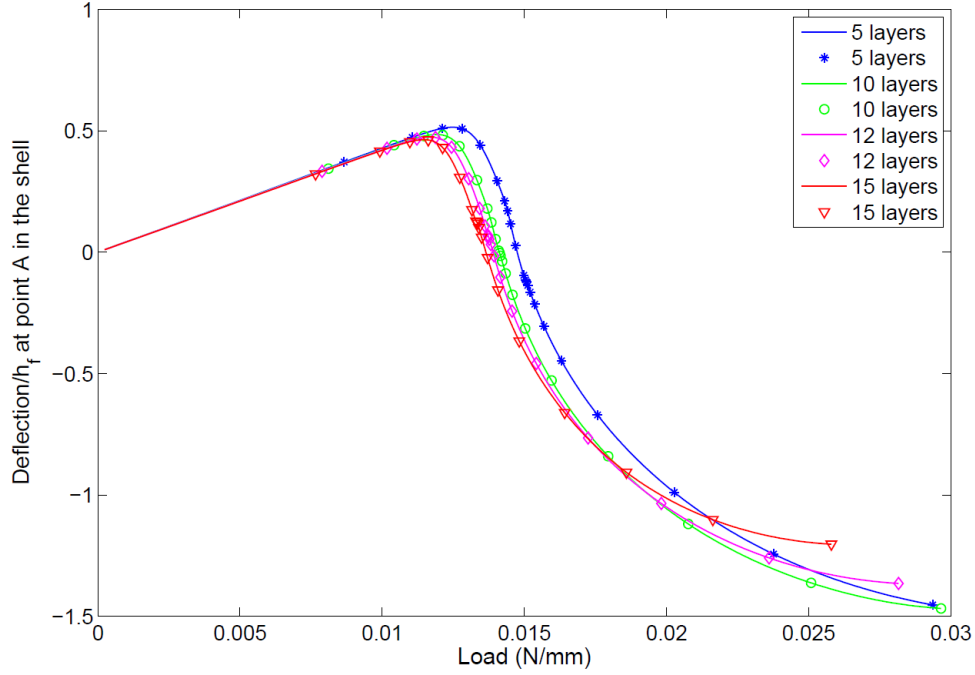
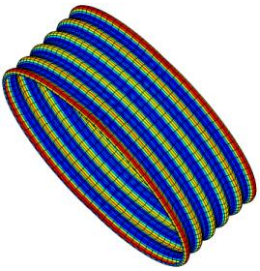
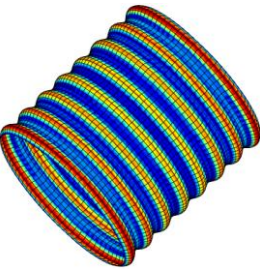
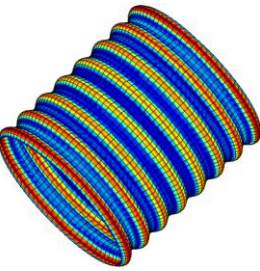

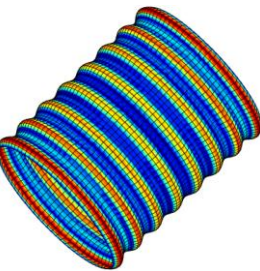
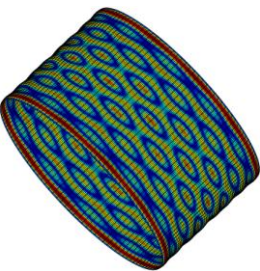


Fig. S1 Convergence test of Core-shell I with  $C_s=3.92$  under axial compression. The core is respectively discretized by 5, 10, 12 and 15 layers in the radial direction. All the post-buckling bifurcation curves share the same trend and similar bifurcation points. ANM parameters:  $n=15$ ,  $\delta=10^{-4}$ . Each point corresponds to one ANM step.

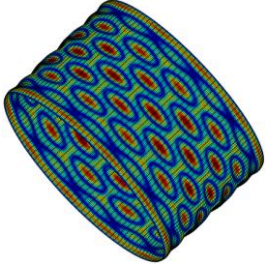
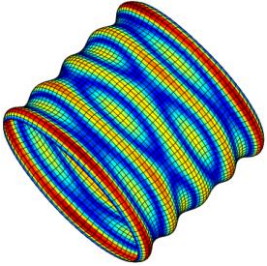
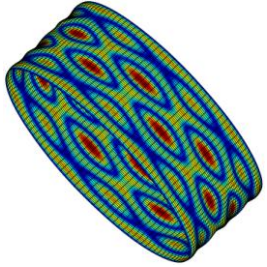
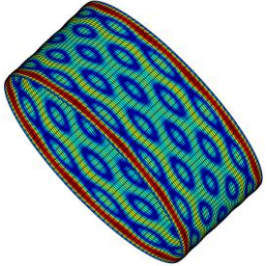
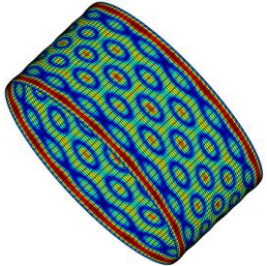
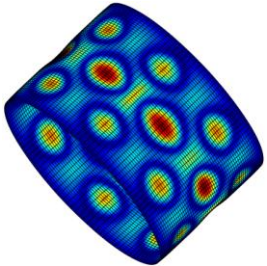
Table S1

Various cases of core-shell cylinders under axial compression to justify the critical value for the phase diagram of Fig. 2 for pattern shapes selected by  $C_s=(E_s/E_f)(R/h_f)^{3/2}$  at the secondary bifurcations (compressive strain  $\gamma_{xx}$  is less than 4% in all the cases and the length  $L$  may vary with the cases).

$C_s$	$R/h_f$	$E_f/E_s$	Patterns
-------	---------	-----------	----------

3.9	200	722	
1	80	722	
0.9	75	722	
0.9	489	12000	
0.8	69	722	
0.8	452	12000	



0.7	413	12000	
0.7	64	722	
0.6	373	12000	
0.5	330	12000	
0.4	300	12000	
0.1	113	12000	

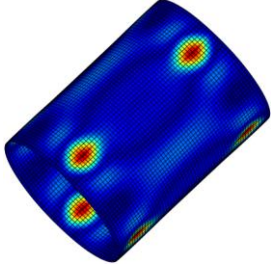

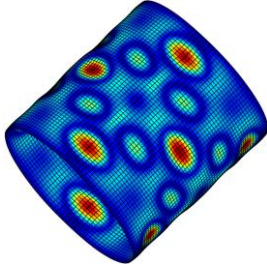

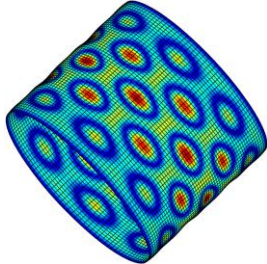
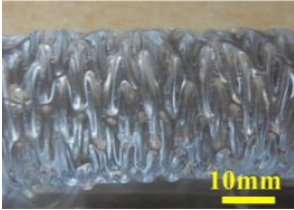
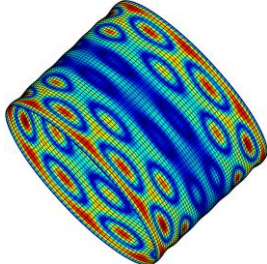

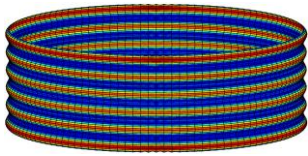
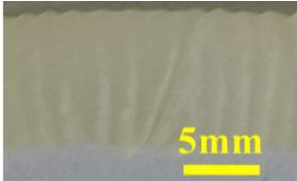
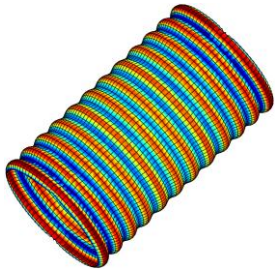
0.01	113	120000	
------	-----	--------	---

Table S2

Comparison of instability patterns between the proposed numerical model and the experiments reported in the supplementary material of Zhao et al. (2014).

$C_s$	$R/h_f$	$E_f/E_s$	Experiments	Numerical results
0.15	70	4000		
0.33	120	4000		
0.71	200	4000		
2	400	4000		

3.77	45	80		
8.12	75	80	